Synsint Research Group

Available online at www.synsint.com

Synthesis and Sintering

ISSN 2564-0186 (Print), **ISSN** 2564-0194 (Online)

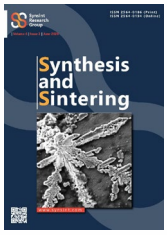

Research article

Corrosion behavior and in-vitro bioactivity of Ti-based composites: Synergistic and competitive effects of ZrO_2 and nHA ceramic reinforcements

Shaghayegh Habibi Anganeh, Vahideh Shahedifar *, Bahereh Tekyeh Marouf

Department of Materials Science and Engineering, Faculty of Engineering, Urmia University, Urmia, Iran

A B S T R A C T

The present study introduces a comparative and synergistic evaluation of corrosion behavior and in-vitro bioactivity of Ti-based composites reinforced with zirconia (ZrO_2) and/or nano-hydroxyapatite (nHA). Pure Ti, Ti–10 vol% nHA (TH), Ti–4 vol% ZrO_2 (TZ), and Ti–4 vol% ZrO_2–6 vol% nHA (TZH) were fabricated via spark plasma sintering (SPS) at 1200 °C under vacuum to elucidate the individual and combined effects of ceramic phases on passive film formation and degradation mechanisms. Potentiodynamic polarization and electrochemical impedance spectroscopy (EIS) were performed after short-term and 14-day immersion in simulated body fluid (SBF). The TH composite exhibited the lowest corrosion current density (9.22×10^{-6} mA/cm^2) and highest polarization resistance (2910 kΩ.cm^2), confirming the formation of a dense, stable Ca–P/TiO_2 multilayer that effectively blocked electrolyte penetration. EIS analysis further revealed the formation of a stable, highly capacitive passive layer on the TH sample, characterized by phase angles near -80° and impedance values up to 1770 kΩ.cm^2. In contrast, the dual-ceramic TZH composite showed micro-galvanic interactions between ZrO_2 and nHA phases, leading to localized pitting and reduced long-term stability. The TZ sample showed delayed but noticeable improvement in corrosion resistance during prolonged immersion, indicating that ZrO_2 contributes to long-term passivation through the gradual formation of a stable ZrO_2-rich barrier. Long−term immersion tests confirmed apatite formation on all samples, with TH exhibiting the most uniform Ca–P-rich layer, as verified by FE-SEM/EDS. Overall, Ti–10 vol% nHA demonstrated superior corrosion resistance and bioactivity, highlighting its strong potential for orthopedic implant applications.

KEYWORDS

Titanium-zirconia-hydroxyapatite composites
Spark plasma sintering (SPS)
Corrosion behavior
Apatite formation
Simulated body fluid (SBF)

OPEN ACCESS

1. Introduction

Titanium and its alloys remain among the most widely used materials for orthopedic and dental implants due to their favorable combination of mechanical strength, corrosion resistance, and biocompatibility [1]. Despite its clinical success, commercially pure titanium (CP Ti) exhibits bioinert behavior and limited osseointegration, and its passive oxide film may degrade in physiological environments containing chloride ions. This challenge has motivated extensive efforts to enhance both corrosion resistance and biological performance through alloying, surface engineering, and ceramic reinforcement such as hydroxyapatite (HA), zirconia [2, 3], and titania [4]. HA provides strong osteoconductivity due to its chemical similarity to bone mineral, whereas ZrO_2 contributes high mechanical stability and chemical inertness. Recent advances in spark plasma sintering (SPS) have enabled the fabrication of dense Ti-ceramic composites with refined

* Corresponding author. *E-mail address:* v.shahedifar@urmia.ac.ir (V. Shahedifar)
Received 20 May 2026; Received in revised form 5 June 2026; Accepted 15 June 2026.

https://doi.org/10.53063/synsint.2026.62342

microstructures and improved interfacial bonding. SPS offers rapid heating, limited grain growth, and reduced porosity, making it a promising route for producing samples with enhanced mechanical and biological properties [5–7].

In the first investigations, rare-earth/calcium phosphate coatings on Ti alloy enhanced corrosion resistance and bioactivity [8]. Then, efforts focused on foundational understanding of corrosion mechanisms and on enhancing biocompatibility through hydroxyapatite coatings. While HA coatings improve osteoconductivity, their brittleness and poor mechanical strength limit long-term durability [9, 10].

The advantages of Ti/HA integration, including effects on hardness, Young's modulus, and corrosion resistance, have been reported by Niespodziana et al. [11]. They used a combination of mechanical alloying and powder metallurgical processes to produce Ti/HA nanostructures. The titanium nanocomposite with 10 vol% HA exhibited higher corrosion resistance, with corrosion current (i_{corr})=1.19×10^{-7} A.cm^{-2} and corrosion potential (E_{corr}) = -0.41 V, compared with pure titanium (i_{corr}=1.31×10^{-5} A.cm^{-2}, E_{corr} = -0.36 V) [11]. Tanigawa et al.'s research on the electrochemical and biological properties of titanium-hydroxyapatite composites fabricated by spark plasma sintering indicated that the titanium composite with 10 wt% hydroxyapatite had the lowest corrosion current density in simulated body fluid (SBF) compared with pure titanium. However, increasing hydroxyapatite to 20 to 30 wt% decreased corrosion resistance due to crater-like defects induced by ceramic particle detachment [12]. Consistent with this, Xie et al. [13] reported decreased corrosion resistance with increased ceramic content, particularly at higher HA loadings, which caused porosity and oxide film discontinuity in Ti-10Mo/HA biocomposites. This heterogeneity and pore formation reduced corrosion resistance. Krishna and Suresh [14, 15] demonstrated that incorporating 5 wt% and 10 wt% nano-hydroxyapatite (nHA) into titanium via powder metallurgy enhanced bioactivity by promoting calcium and phosphate mineral phase deposition. The presence of nano-HA contributed to higher cell regeneration and growth rates. They also observed higher surface energies for the composites than for medical-grade pure Ti. All the samples were nontoxic against 3T3 cells, as observed from the cytotoxicity test using the MTT assay. The electrochemical behavior of a titanium-alumina biocomposite after 1 hour and 24 hours of immersion in Ringer's solution was examined by Bahrami Nasseb et al. [16]. Results showed that the corrosion resistance of Ti-25 wt% Al_2O_3 increased with immersion time. In another study, researchers examined the mechanical and corrosion properties of a titanium-based composite material enhanced by the addition of alumina and hydroxyapatite. The addition of alumina alone reduced the compressive strength of the samples. However, adding hydroxyapatite to this composite increased the compressive strength. This increase in strength is attributed to the filling of cavities and a decrease in porosity in the material's structure. Corrosion tests showed that adding alumina and hydroxyapatite to pure titanium significantly increased its corrosion resistance in Ringer's solution. This increase in corrosion resistance is attributed to the formation of an oxidized layer on the surface of the material [17]. In another study, researchers observed that adding ZrO_2 significantly improved the corrosion resistance of Ti-12Mo nanocomposites. This is due to the lower reactivity of ZrO_2 ceramic particles, which are resistant to most corrosive environments. Also, the good distribution of these particles in the matrix as an internal passive material helps to reduce corrosion. The lowest corrosion rate was observed in the nanocomposite Ti-12Mo/5% ZrO_2. This can be attributed to full density and the absence of porosity. The presence of porosity contributes to the penetration of the corrosive substance into the sample [18].

Despite numerous studies on binary Ti–HA or Ti–ZrO_2 composites, comparative investigations into the synergistic or competitive effects of combining both reinforcements in a titanium matrix remain scarce. Understanding how HA and ZrO_2—individually or together—affect corrosion behavior, passive film stability, and in-vitro bioactivity is crucial for optimizing next-generation implant materials.

Therefore, the present study systematically evaluates the corrosion resistance and bioactivity of SPS-fabricated Ti, Ti–10 vol% nHA, Ti–4 vol% ZrO_2, and Ti–4 vol% ZrO_2–6 vol% nHA composites. Potentiodynamic polarization, electrochemical impedance spectroscopy, and long-term immersion in simulated body fluid (SBF) were employed to elucidate the role of each ceramic phase in passive film formation and apatite deposition. By correlating electrochemical performance with microstructural features, this work aims to clarify the mechanisms through which HA and ZrO_2 influence the degradation behavior of titanium and to identify compositions with optimal potential for orthopedic implant applications.

2. Materials procedure

2.1. Synthesis of nHA

Nanohydroxyapatite (nHA) powder was synthesized using a sol–gel route. In this method, a 0.5 M ethanol solution of phosphorus pentoxide (P_2O_5) was added dropwise into a 1.67 M solution of calcium nitrate tetrahydrate ($Ca(NO_3)_2.4H_2O$) under continuous stirring for 3 h. The controlled dropwise addition was employed to ensure homogeneous nucleation and prevent premature precipitation, thereby improving the chemical uniformity of the final gel. The reaction proceeded according to the following equation:

$$10Ca(NO_3)_2.4H_2O + 3P_2O_5 \rightarrow Ca_{10}(PO_4)_6(OH)_2 + 18H_2O \quad (1)$$

The resulting mixture was dried at 60 °C for 48 h to remove residual solvent. Subsequently, the dried gel was calcined at 650 °C for 3 h to enhance crystallinity and eliminate organic residues, yielding a fine, white, and phase-pure nHA powder.

2.2. Preparation of samples

Commercially pure titanium (hexagonal phase, particle size less than 45 µm, purity over 99%, sourced from Belgium), zirconia (monoclinic phase, average particle size of 3 µm, purity exceeding 99%, from Afagh Ceramic Co.), and the synthesized nHA were used as starting materials. Fig. 1 shows SEM images and X-ray diffraction (XRD) patterns of the as-received powders. Titanium particles are angular and non-spherical, with varying sizes, indicating a broad particle size distribution (Fig. 1a). Zirconia powders are also not uniform in size. They consist of fine and coarse particles (Fig. 1c).

The powders were weighed to achieve the desired compositions and then milled in a planetary ball mill (Amin Asia MPM2*250H, Iran) at 300 rpm for 1 h with a ball-to-powder ratio of 10:1. Zirconia milling media (5 mm) were used to minimize contamination and ensure efficient energy transfer during mixing. All milling operations were performed in a hardened steel container under an argon atmosphere to prevent titanium oxidation. For compositions containing nanohydroxyapatite, the nanopowder was first dispersed in ethanol using an ultrasonic bath (Sonicator Q500, USA) at 265 W for 20 min.

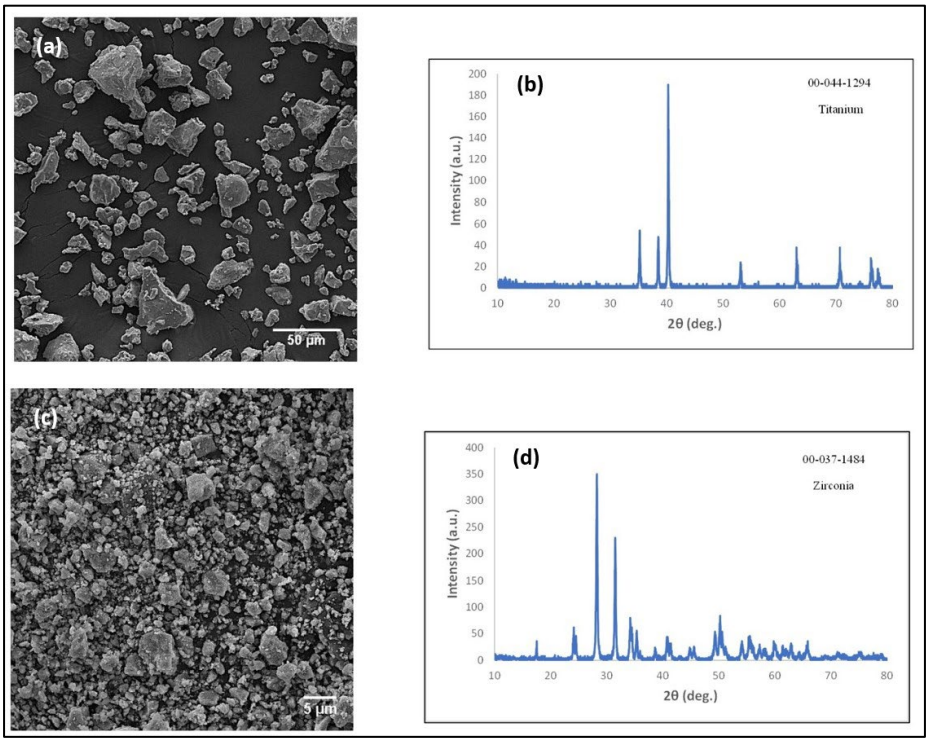

Fig. 1. SEM images and XRD patterns of a, b) the purchased pure titanium powder and c, d) commercially zirconia powder.

This pre-dispersion step was essential to break agglomerates and promote the uniform distribution of nanoparticles within the titanium matrix. The mixed slurry was then dried in an oven (Tebazma HMS 14, Iran) at 110 °C for 6 h. Sintering was performed by spark plasma sintering (SPS 20T 10, China) at 1200 °C for 10 min under a uniaxial pressure of 40 MPa in vacuum. The final samples were designated as T (pure Ti), TZ (Ti–4 vol% ZrO_2), TH (Ti–10 vol% nHA), and TZH (Ti–4 vol% ZrO_2–6 vol% nHA). Fig. 2 shows a schematic of the materials preparation procedure.

2.3. Characterization techniques

Phase analysis was conducted using an X-ray diffractometer (XRD: Philips, PW 1800, operating at 40 kV and 30 mA). The XRD pattern of the samples was obtained using monochromatic CuKα radiation in the

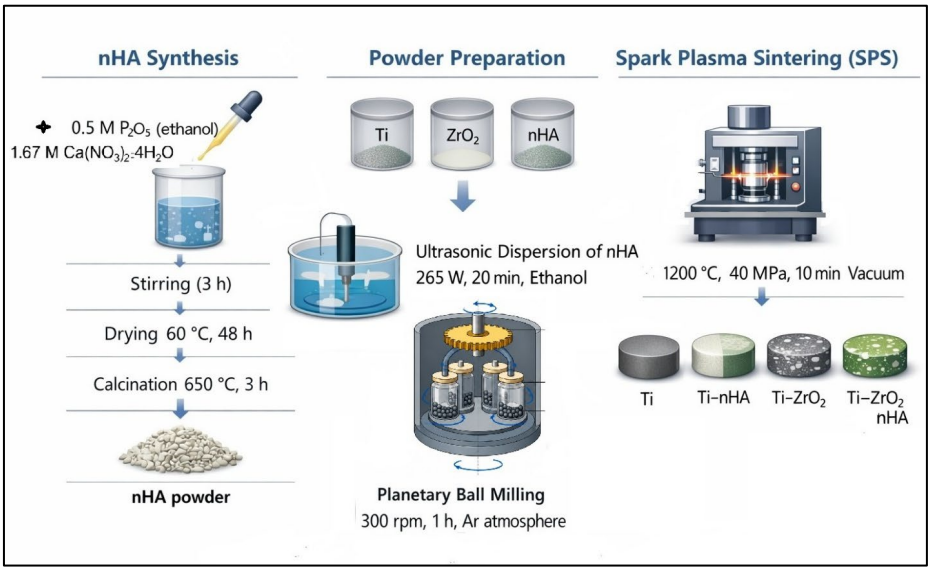

Fig. 2. Schematic illustration of the materials preparation procedure.

range of 10 to 90 degrees. A step size of 0.04 degrees and a scan step time of 1 second were used. Phase identification was performed using X'Pert HighScore Plus software 3.0.5 to ensure accurate detection of minor phases. The morphology of synthesized nHA and received powders was examined using field-emission scanning electron microscopy (FESEM; TESCAN Mira3, Czech Republic). Elemental composition was analyzed via energy-dispersive spectroscopy (EDS; DXP-X10P). Particle size distribution of nHA was measured using ImageJ 1.44p and confirmed by dynamic light scattering (DLS).

Electrochemical corrosion behavior was evaluated in simulated body fluid (SBF) using an electrochemical workstation (AUTOLAB PGSTAT30, Netherlands) at room temperature. Polarization curves and electrochemical impedance spectroscopy (EIS) were recorded to determine corrosion potential, corrosion current density, polarization resistance, and passive film characteristics. The exposed surface area of each specimen was 1.76 cm^2. The electrolyte composition of the used SBF is shown in Table 1.

In-vitro immersion tests were performed according to ASTM G31-72 [18], where each specimen was immersed in 90 ml of SBF at 37 °C for 14 days. After immersion, surface apatite formation was examined using FE-SEM/EDS.

Table 1. Ion concentrations of SBF and human blood plasma.

Ion	Concentration of SBF (10^{-3} mol) at pH 7.4	Concentration of blood plasma (10^{-3} mol) at pH 7.2–7.4
Na^+	142.0	142.0
K^+	5.0	5.0
Mg^{2+}	1.5	1.5
Ca^{2+}	2.5	2.5
Cl^-	147.8	103.0
HCO_3^-	4.2	27.0
HPO_4^{2-}	1.0	1.0
SO_4^{2-}	0.5	0.5

3. Results and discussion

3.1. Powder analysis

Fig. 3 shows the SEM image and XRD pattern of the hydroxyapatite synthesized by the sol-gel method. By comparing the observed peaks with the standard card number 00-009-0432, it was confirmed that the synthesized powder corresponds to single-phase crystalline HA, and no secondary or impurity phases were detected. The absence of parasitic phases such as TCP or CaO is particularly important, since these phases can alter dissolution kinetics in SBF and destabilize the interfacial chemistry when HA is embedded in a Ti [19]. The mean particle size of the nHA measured from the SEM image using ImageJ was 24.5 ± 6.5 nm with a narrow distribution, indicating nanometric, relatively spherical, and homogeneous particles. Such a narrow size distribution at the nanoscale is expected to increase the specific surface area, promote faster ion exchange (Ca^{2+}, PO_4^{3-}) with the surrounding medium, and facilitate apatite nucleation during in-vitro tests [20]. However, due to the high surface energy of nanoparticles, some agglomeration was observed in the SEM micrographs. This agglomeration can lead to local inhomogeneities, increased porosity, and reduced effective surface area if not properly dispersed. Hence, before applying to make a sample, the nHA particles were dispersed in ethanol for 20 min using an ultrasonic bath. Additionally, this pre-dispersion step is critical to avoid the formation of weak, porous regions that could act as preferential corrosion paths.

To further validate the particle size, DLS (dynamic light scattering) analysis (Fig. 4) was performed, yielding an average size of 26 ± 1.1 nm, in good agreement with SEM results. The consistency between SEM-and DLS-derived sizes confirms that the sol–gel route produced stable nHA particles without significant large aggregates in suspension.

3.2. Tafel polarization and electrochemical impedance spectroscopy after 1 h immersion in SBF

The potentiodynamic polarization curves of T, TH, TZ, and TZH samples in SBF after 1 h immersion at 24.1 °C are presented in Fig. 5. These curves illustrate the relationship between the corrosion potential

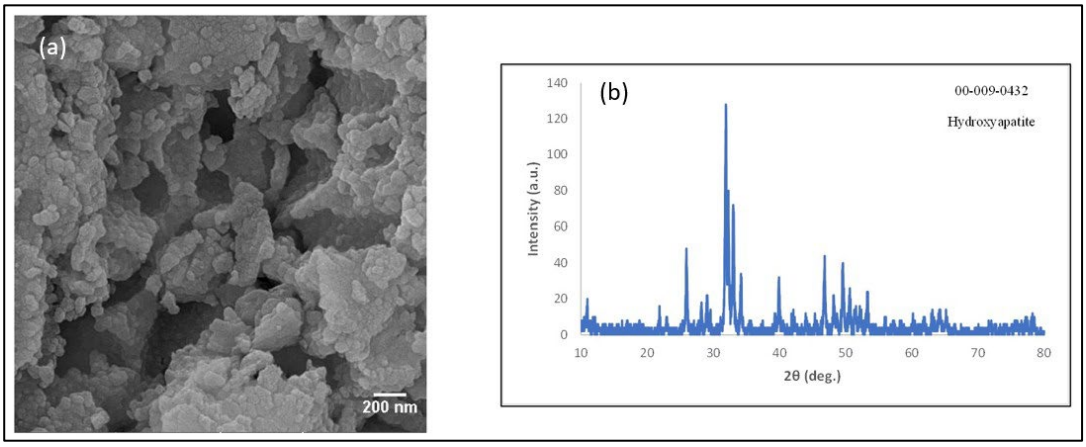

Fig. 3. a) SEM image and b) XRD pattern of hydroxyapatite nanoparticles synthesized by the sol-gel method.

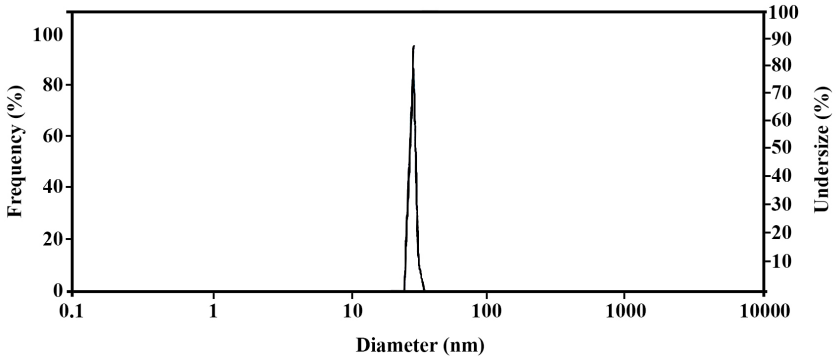

Fig. 4. The mean particle size and distribution of synthesized nHA by the DLS method.

and the density of corrosion current. A higher density of corrosion current indicates a higher corrosion rate and, consequently, lower corrosion resistance. Electrochemical parameters, including corrosion current (i_{corr}), corrosion potential (E_{corr}), polarization resistance (R_p calculated using the Stern- Geary formula), and corrosion rate for the samples, are summarized in Table 2.

The results show that the E_{corr} of the T sample is more positive (-282 mV) than that of the other samples. This is due to the higher thermodynamic stability of titanium oxide. The addition of nHA alone, or in combination with ZrO_2, improved the corrosion resistance of the Ti-nHA and Ti-ZrO_2-nHA samples compared to pure Ti by reducing the corrosion current density and enhancing polarization resistance. So that in the TH sample, upon addition of 10 vol% nHA, i_{corr} decreases from 3.07×10^{-5} mA/cm^2 for the T sample to 1.53×10^{-5} mA/cm^2 and R_p increases from 583 kΩ.cm^2 for the T sample to 2123 kΩ.cm^2, indicating a substantial improvement in corrosion resistance at short immersion times. This behavior suggests that nHA contributes to the rapid formation of a protective surface layer, likely involving both TiO_2 and Ca–P rich phases, which act as a barrier to ionic transport.

In contrast, the TZ sample (Ti–ZrO_2) shows a higher corrosion current density (6.25×10^{-5} mA/cm^2) and lower R_p (279 kΩ.cm^2) compared to pure Ti. This indicates that, within the first hour of immersion, the presence of ZrO_2 alone does not yet translate into an effective protective layer, possibly because the ceramic–metal interfaces and residual porosity facilitate localized electrolyte penetration before a stable passive film is established. The TZH sample exhibits intermediate behavior, with $i_{corr} = 1.88 \times 10^{-5}$ mA/cm^2 and R_p = 797 kΩ.cm^2, suggesting a competition between beneficial nHA-induced passivation and microstructural complexity introduced by the dual-ceramic system.

Electrochemical impedance spectroscopy (EIS) provides further insight into corrosion mechanisms. EIS offers quick, accurate tools for evaluating the material/solution interface. Fig. 6 shows Nyquist plots for the T, TH, TZ, and TZH samples, with symbols and lines representing the experimental and fitted results, respectively. Nyquist plots for all samples show incomplete capacitive semicircles across the entire frequency range, characteristic of passive behavior with high surface resistance. The semicircle diameter, proportional to the charge-transfer resistance, is largest for TH and TZH, confirming their superior resistance to charge transfer at the metal/electrolyte interface compared to T and TZ. This is consistent with the higher R_p values obtained from Tafel analysis. The larger diameter suggests a more insulating, thicker, and more protective passive film on the surface [21].

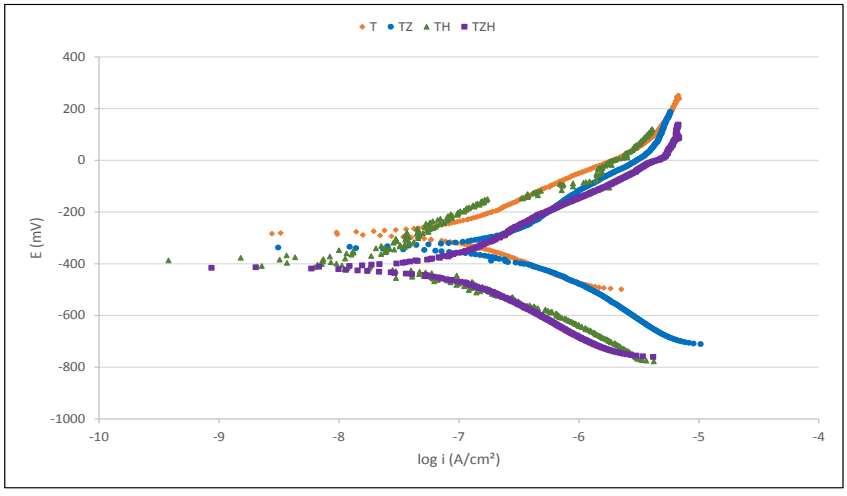

Fig. 5. The potentiodynamic polarization curves of T, TH, TZ, and TZH samples in SBF after 1 h of immersion.

Table 2. Electrochemical parameters of T, TH, TZ, and TZH samples in SBF after 1 h immersion.

Sample	E_{corr} (mV)	i_{corr} (mA/cm^2)	Slope of anodic region (β_a) (mV/dec)	Slope of cathodic region ($-\beta_c$) (mV/dec)	R_p (kΩ.cm^2)	Corrosion Rate (mm/year)
T	-282	3.07×10^{-5}	89	77	583	2.67×10^{-4}
TH	-385	1.53×10^{-5}	224	112	2123	1.77×10^{-4}
TZ	-339	6.25×10^{-5}	90.9	72	279	5.45×10^{-4}
TZH	-417	1.88×10^{-5}	74	65	797	1.64×10^{-4}

The Bode complex planes show how the magnitude of impedance and the phase angle vary with the logarithm of frequency. At high frequencies, the influence of electrolyte resistance, R_s, is dominant in the total impedance. At medium frequencies, the capacitive behavior of the electrode is expressed [21]. At low frequencies, the impedance value is related to the system's resistance (the sum of all resistances). Based on Bode plots (Fig. 7), the TH sample exhibits the highest impedance modulus at low and medium frequencies with the slope of approximately -1 and a phase angle approaching -80 °, indicative of a highly capacitive and well-developed passive film. The presence of two time constants in the phase angle response of TH suggests the coexistence of an inner compact oxide layer and an outer, more porous Ca–P rich layer, both contributing to the overall corrosion protection. In contrast, the TZ sample shows lower impedance and a less pronounced capacitive response, reflecting a less effective barrier layer at this early stage.

To quantitatively interpret the EIS data, equivalent circuits were used (Fig. 8). This circuit includes capacitors and resistors that represent the electrical and physical properties of the electrochemical interface. Surface roughness and defects decrease the efficiency of an ideal capacitor in modeling the surface double layer. In such cases, a constant phase element (CPE) replaces the ideal capacitor, with its impedance, Z_{CPE}, described by the following equation:

$$Z_{CPE} = \frac{1}{Y_0 (j\omega)^n} \quad (2)$$

where j is an imaginary number (j = √-1), ω is the circular frequency, Y_0 and n are parameters of the constant phase element. The CPE exponent, n, is a number between zero and one. In n=1, capacitive behavior and n=0 resistive behavior are obtained. The deviation of n from unity reflects surface heterogeneity and roughness. Normally, a low Y_0 value means a good and high-quality film surface.

By adjusting the measured frequency dependence of the impedance with the theoretical impedance function for the proposed equivalent circuit, the values of charge transfer resistance (R_{CT}), oxide layer (corrosion products) resistance (R_1), resistance of oxide layer (corrosion products)/metal interface (R_2), solution resistance (R_s), Warberg diffusion coefficient (W) and doble-layer capacitance (C_{dl}) were determined (Table 3). The values of the chi-square (χ^2) statistic are minimal, indicating the high quality of the fitted results.

The effective capacitance (C) was calculated using the following equation:

$$C = Y_0^{\frac{1}{n}} R^{\frac{1-n}{n}} \quad (3)$$

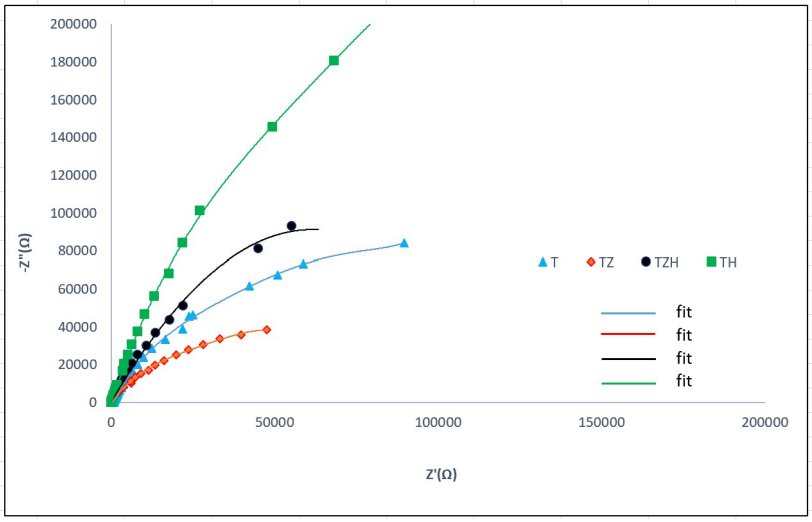

Fig. 6. Nyquist plots of the T, TH, TZ, and TZH samples in SBF after 1 h immersion.

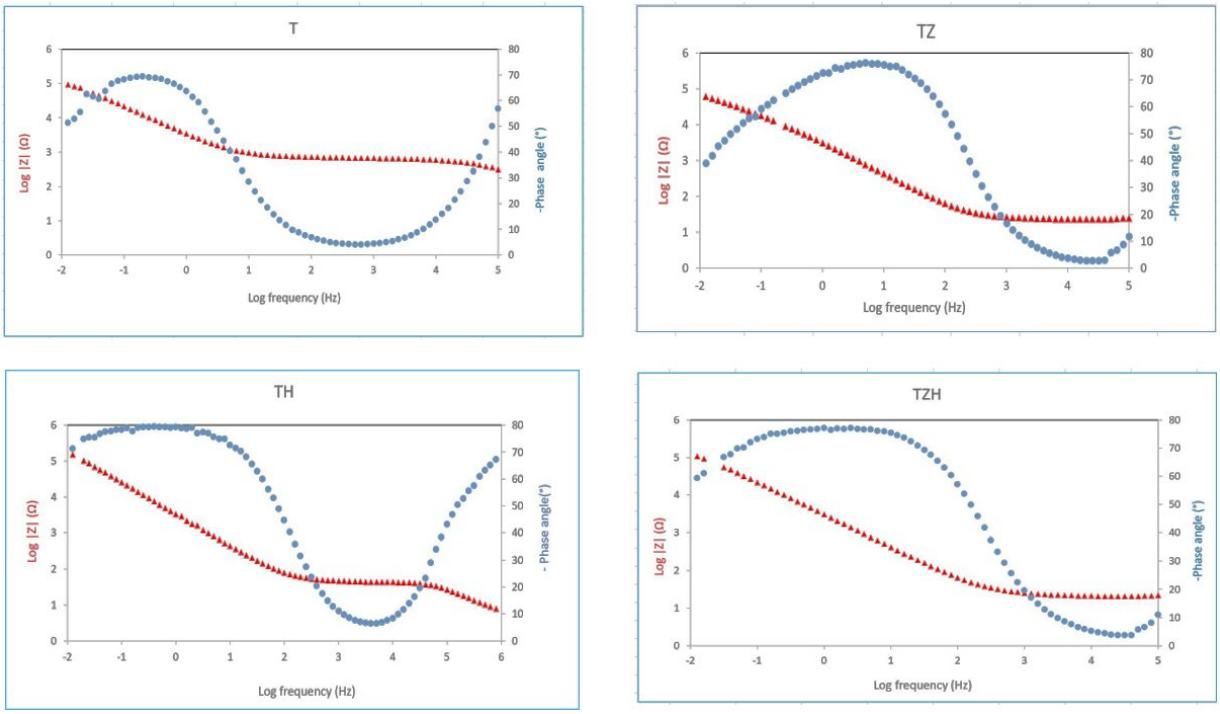

Fig. 7. Bode phase plots recorded on the T, TH, TZ, and TZH samples in SBF after 1 h of immersion.

The high values of double-layer capacitance (C_{dl}) in the TZH sample and the outer layer capacitance (C_1), as well as low value capacitance of outer layer/metal interface (C_2) in the TZ sample, suggest the presence of electrolytes on the surface. In other words, when the electrolyte passes through the porous surface layer, it increases the dielectric coefficient of the equivalent capacitors, leading to relatively high equivalent capacitance values for the surface and outer layer. Table 3 shows that the lowest outer layer capacitance values are for T and TH samples, indicating fewer electrolytes on their surfaces. Also, lower Y_0 and higher n values for TH indicate a more homogeneous and compact passive film, whereas higher Y_0 values for TZ and TZH point to increased electrolyte penetration and a more defective surface layer. The presence of a Warburg element (W) in some fits suggests diffusion-controlled processes, particularly in samples where electrolyte can access subsurface regions through pores or microcracks.

3.3. Tafel polarization and electrochemical impedance spectroscopy after 14 days of immersion in SBF

The potentiodynamic polarization curves of T, TH, TZ, and TZH samples in SBF after 14 days of immersion are presented in Fig. 9, and the corresponding electrochemical parameters are summarized in Table 4. After 14 days of immersion in SBF, a significant evolution of the electrochemical behavior is observed. The TH sample exhibits the lowest corrosion current density (9.22×10^{-6} mA/cm^2) and the highest polarization resistance (2910 kΩ.cm^2), representing a marked improvement compared to its 1 h performance. This long-term enhancement indicates that nHA not only contributes to initial passivation but also supports the progressive growth of a dense, adherent Ca–P-rich layer that seals surface defects and stabilizes the underlying TiO_2 film. The corrosion rate of TH is

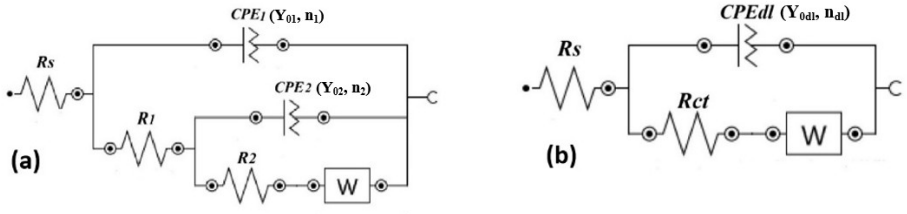

Fig. 8. Equivalent circuit for a) T, TH, and TZ samples and b) TZH sample.

Table 3. Electrical parameters of the equivalent circuit obtained by fitting the experimental results of EIS for the T, TH, TZ, and TZH samples in SBF.

	T	TZ	TH	TZH
R_s ($\Omega.cm^2$)	-	42.24	4.25	35.2
R_1 ($\Omega.cm^2$)	1170.4	27632	74.34	-
Y_{01} ($\Omega^{-1} s^n cm^{-2}$)	20.57×10^{-9}	33.92×10^{-6}	25.99×10^{-9}	-
n_1	0.841	0.885	0.9	-
C_1 ($F.cm^{-2}$)	2.75×10^{-9}	33.63×10^{-6}	6.02×10^{-9}	-
R_2 ($\Omega.cm^2$)	316800	1584	1770000	-
Y_{02} ($\Omega^{-1} s^n cm^{-2}$)	37.9×10^{-6}	3.69×10^{-6}	33.22×10^{-6}	-
n_2	0.835	0	0.882	-
C_2 ($F.cm^{-2}$)	61.93×10^{-6}	0	57.29×10^{-6}	-
W ($\Omega^{-1} s^{1/2} cm^{-2}$)	50.79×10^{-6}	21.25×10^{-6}	-	25.91×10^{-6}
R_{ct} ($\Omega.cm^2$)	-	-	-	461120
Y_{0dl} ($\Omega^{-1} s^n cm^{-2}$)	-	-	-	38.86×10^{-6}
n_{dl}	-	-	-	0.856
C_{dl} ($F.cm^{-2}$)	-	-	-	63.14×10^{-6}
χ^2	2.1×10^{-3}	4.3×10^{-3}	19×10^{-3}	6×10^{-3}

reduced to 1.07×10^{-4} mm/year (40% reduction compared to 1 h immersion), confirming its superior durability in simulated physiological conditions.

Interestingly, the TZ sample, which initially showed inferior behavior, now displays a significant improvement, with $i_{corr} = 1.44 \times 10^{-5}$ mA/cm^2 and R_p = 1341 kΩ.cm^2. This suggests that ZrO_2 requires longer immersion times to develop a protective effect, likely through the formation of a stable ZrO_2-rich passive layer [18, 22] and improved blocking of active sites at the Ti/ZrO_2 interfaces. The more positive corrosion potential of TZ (-275 mV) compared to T (-545 mV) further supports the enhanced thermodynamic stability of its passive film after prolonged exposure.

In contrast, the TZH sample shows the highest corrosion current density (1.57×10^{-4} mA/cm^2) and the lowest R_p (113.3 kΩ.cm^2) after 14 days, indicating a deterioration in corrosion resistance. This behavior can be attributed to the complex microstructure of the dual-ceramic composite, where the simultaneous presence of micron-sized ZrO_2 and nHA may create microgalvanic cells, interfacial debonding, and percolation paths for electrolyte penetration, especially if agglomeration or poor bonding occurs. The accumulation of nHA around ZrO_2 particles can generate local porosity and weaken the integrity of the passive layer.

Nyquist plots after 14 days (Fig. 10) show that the TH sample has the largest semicircle, consistent with the highest total resistance extracted from equivalent circuit fitting (Table 5). According to Table 5, the total resistance, including apatite layer resistance (R_1), the resistance of corrosion product/oxide layer interface (R_2), and the resistance of oxide layer/metal interface (R_3) for the TH sample, reaches approximately 16 MΩ·cm², far exceeding that of the other samples, which confirms the formation of a highly resistive, multi-layered barrier against charge transfer and ionic diffusion.

Bode phase plots (Fig. 11) reveal three distinct peaks for TH, indicating three time constants associated with: (i) the outer apatite layer, (ii) the intermediate corrosion product/oxide layer, and (iii) the metal/oxide interface. This complex but stable stratified structure is responsible for its excellent long-term corrosion resistance compared to the other samples.

Table 4. Electrochemical parameters of T, TH, TZ, and TZH samples in SBF after 14 days of immersion.

Sample	E_{corr} (mV)	i_{corr} (mA/cm^2)	β_a (mV/dec)	$-\beta_c$ (mV/dec)	R_p (kΩ.cm^2)	Corrosion rate (mm/year)
T	-545	3.71×10^{-5}	92	75.4	485	3.2×10^{-4}
TH	-457	9.22×10^{-6}	145.6	107.3	2910	1.07×10^{-4}
TZ	-275	1.44×10^{-5}	82.4	97.6	1341	1.26×10^{-4}
TZH	-745	1.57×10^{-4}	89	76	113.3	13.7×10^{-4}

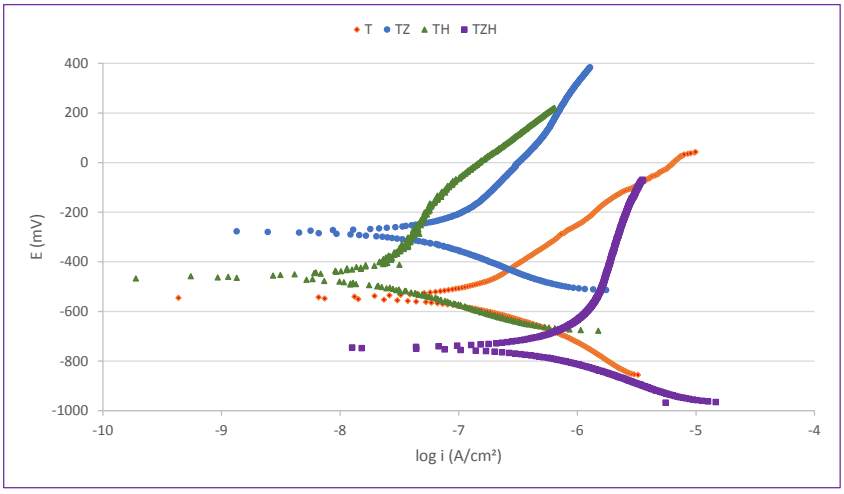

Fig. 9. The potentiodynamic polarization curves of T, TH, TZ, and TZH samples in SBF after 14 days of immersion.

For TZH, the broader and lower phase-angle peak suggests a less protective and more heterogeneous surface layer.

Fig. 12 illustrates the equivalent circuits used to analyze the impedance data for all samples in SBF after 14 days of immersion.

According to Table 5, the higher outer-layer capacitance value for TZH, derived from the CPE parameters, implies an increased dielectric constant due to electrolyte penetration into surface pores, which is consistent with its higher corrosion rate. The presence of a Warburg element in TZH also indicates diffusion-controlled processes through a porous or cracked layer, further compromising its protective performance.

Schematic illustration of corrosion evolution for T, TZ, TH, and TZH samples after immersion in SBF for 1 h and 14 days is shown in Fig. 13. (a) Pure Ti: At short immersion, a thin TiO_2 passive film allows rapid ion ingress and localized corrosion. After 14 days, oxide breakdown and pitting occur, accompanied by hydrogen evolution and deeper Cl^- penetration. (b) Ti-ZrO_2 composite: Initially, a porous TiO_2/ZrO_2 layer forms with localized corrosion and low charge-transfer resistance. After 14 days, a dense ZrO_2-rich protective film develops, reducing ion ingress and improving electrochemical stability. (c) Ti-nHA composite: A thin TiO_2/Ca–P layer forms initially. Long-term immersion leads to the growth of a dense multi-layered TiO_2 + Ca–

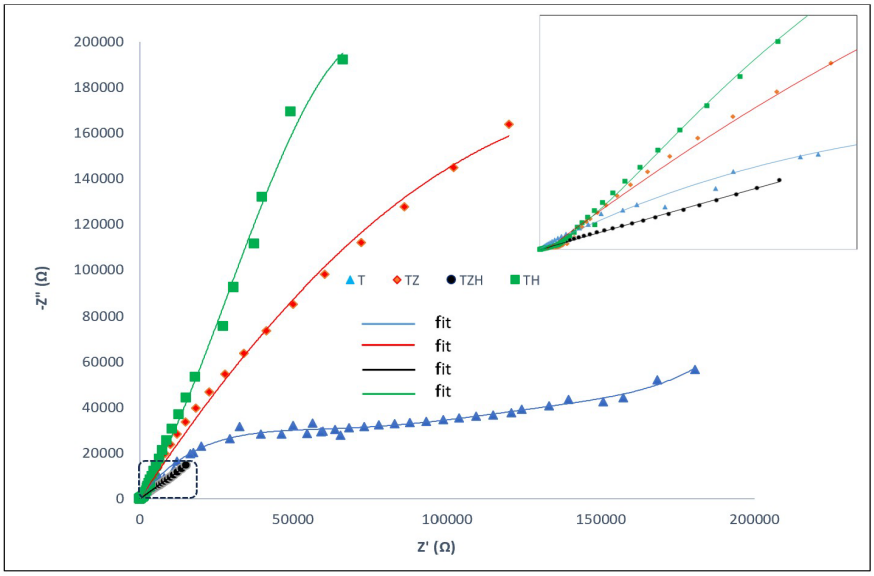

Fig. 10. Nyquist plots of the T, TH, TZ, and TZH samples in SBF after 14 days of immersion (insert: zoomed high-frequency part of impedance spectra).

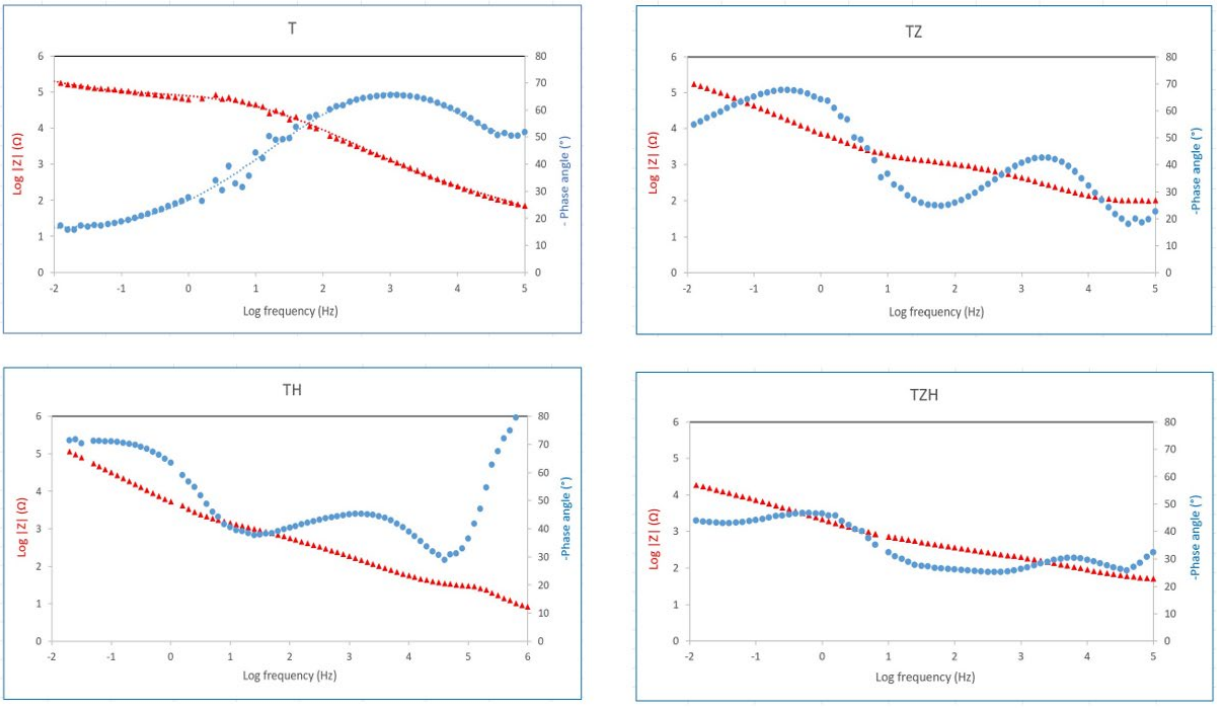

Fig. 11. Bode phase plots recorded on the T, TH, TZ, and TZH samples in SBF after 14 days of immersion.

P + apatite film, providing strong passivation and bioactive surface stability. (d) Ti-ZrO_2-nHA composite: The early stage shows a heterogeneous TiO_2/ZrO_2/HA layer with micro-galvanic activity at interphase boundaries. After 14 days, the layer degrades, and deep pitting occurs due to galvanic coupling between ZrO_2 and HA phases; Ti^{4+}/Zr^{4+}/Ca^{2+} ions are released, leading to severe degradation.

3.4. In-vitro bioactivity

The in-vitro bioactivity of the composites was evaluated by immersing the samples in SBF for 14 days and examining the surfaces by FESEM/EDS (Fig. 14). All samples exhibited apatite precipitation, confirming their ability to induce bioactive responses under simulated physiological conditions. However, the TH sample (Ti–10 vol% nHA) showed the highest density and most uniform coverage of apatite nodules, forming a continuous layer that almost fully covered the surface. This indicates that the presence of nHA within the Ti matrix significantly enhances the nucleation and growth of bone-like apatite. Other researchers have also stated that hydroxyapatite nanoparticles can increase the surface energy of the composite and potentially lead to better wettability and more apatite precipitation [23, 24].

EDS analysis of the precipitated layers revealed strong Ca and P signals on the TH sample (Fig. 15), with a Ca/P weight ratio of 2.12, which is close to that of stoichiometric hydroxyapatite in bone tissue, i.e, 2.16 [25]. The high surface energy and chemical affinity of nHA for Ca^{2+} and PO_4^{3-} ions in SBF promote rapid formation of a Ca–P-rich layer, which not only improves bioactivity but also contributes to corrosion protection by acting as an additional physical barrier. In the case of the pure Ti and TZ samples, apatite formation was less dense and more localized, suggesting a slower bioactive response and fewer nucleation sites than the TH sample. For the TZH sample, apatite deposition was observed but appeared less uniform and more discontinuous than on TH.

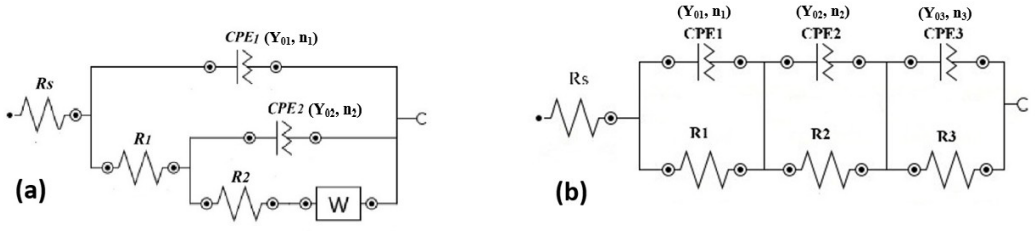

Fig. 12. Equivalent circuit for a) T, TZ, and TZH samples and b) TH sample.

Table 5. Electrical parameters of the equivalent circuit obtained by fitting the experimental results of EIS for the T, TH, TZ, and TZH samples in SBF.

	T	TZ	TH	TZH
R_s ($\Omega.cm^2$)	67.05	146.08	2.99	58.08
R_1 ($\Omega.cm^2$)	52800	2376	36.3	686.4
Y_{01} ($\Omega^{-1} s^n cm^{-2}$)	412.5×10^{-9}	2.65×10^{-6}	27.46×10^{-9}	15.79×10^{-6}
n_1	0.785	0.703	1	0.559
C_1 ($F.cm^{-2}$)	0.14×10^{-6}	0.31×10^{-6}	27.46×10^{-9}	0.44×10^{-6}
R_2 ($\Omega.cm^2$)	1760	872960	6372	27632
Y_{02} ($\Omega^{-1} s^n cm^{-2}$)	7.21×10^{-6}	16.13×10^{-6}	30.85×10^{-6}	69.88×10^{-6}
n_2	0.22	0.807	0.552	0.629
C_2 ($F.cm^{-2}$)	1.36×10^{-12}	30.36×10^{-6}	8.24×10^{-6}	103.02×10^{-6}
W ($\Omega^{-1} s^{1/2} cm^{-2}$)	0.51×10^{-9}	19.43×10^{-6}	-	63.63×10^{-6}
R_3 ($\Omega.cm^2$)	-	-	1593×10^4	-
Y_{03} ($\Omega^{-1} s^n cm^{-2}$)	-	-	27.29×10^{-6}	-
n_3	-	-	0.833	-
C_3 ($F.cm^{-2}$)	-	-	92.24×10^{-6}	-
χ^2	2.7×10^{-3}	3.1×10^{-3}	3.38×10^{-3}	2.1×10^{-3}

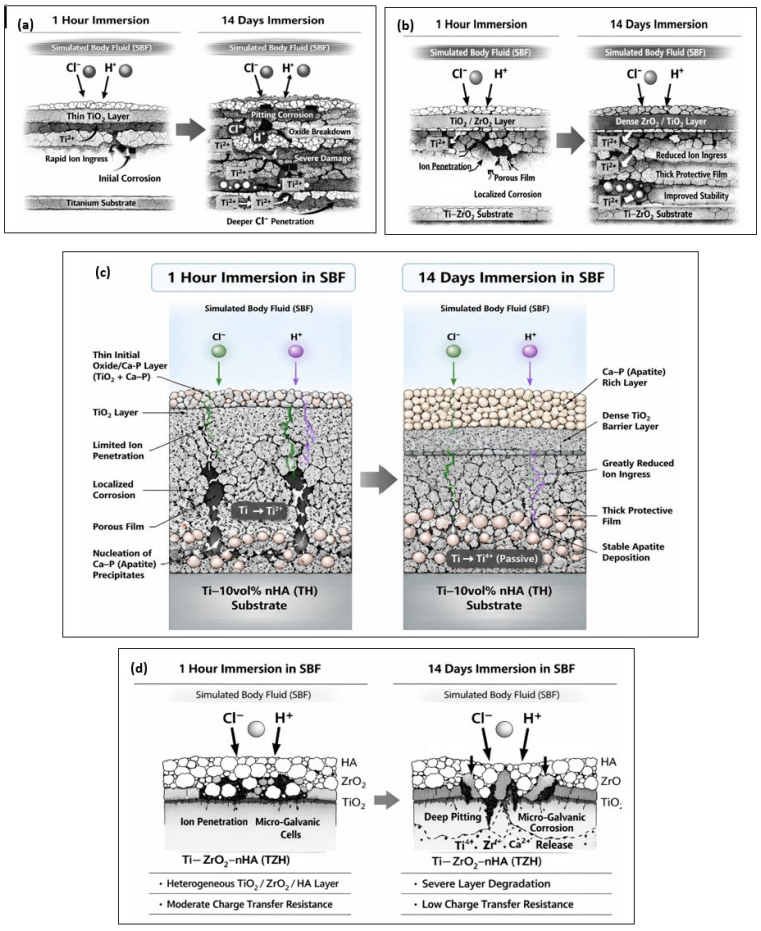

Fig. 13. Schematic illustration of corrosion evolution for a) T, b) TZ, c) TH, and d) TZH samples after immersion in SBF for 1 h and 14 days.

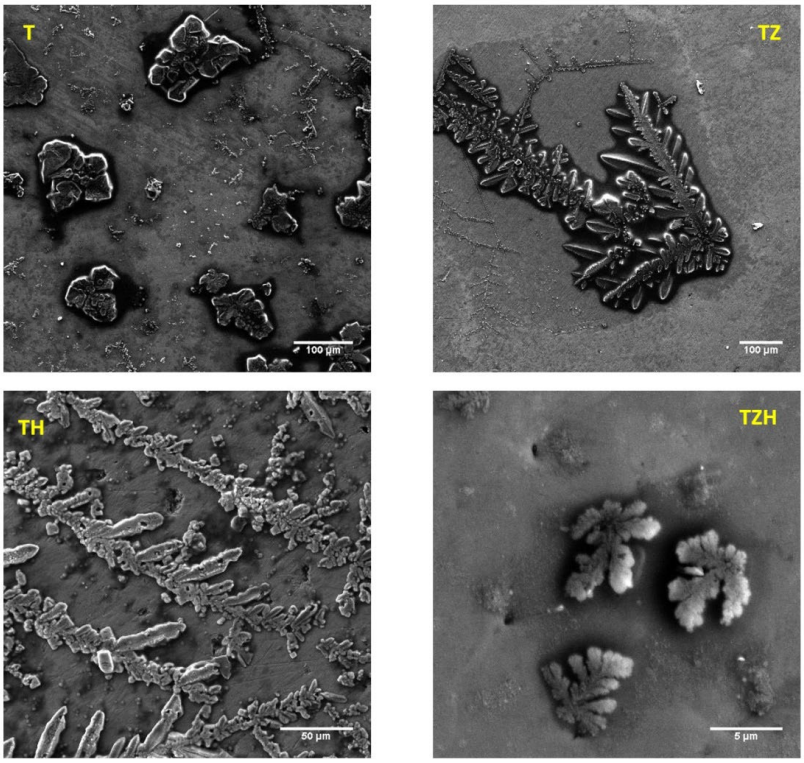

Fig. 14. SEM images of the surfaces of T, TH, TZ, and TZH samples in SBF after 14 days of immersion.

4. Conclusions

This work investigated the corrosion behavior and in-vitro bioactivity of SPS−fabricated Ti-based composites reinforced with zirconia and/or nano−hydroxyapatite. The sol–gel synthesis route successfully produced phase−pure nHA nanoparticles. The results demonstrated that incorporating 10 vol% nHA into commercially pure titanium (TH sample) produced the most significant enhancement in both short-term and long-term corrosion resistance, as evidenced by the lowest corrosion current densities, highest polarization resistances, and the largest Nyquist semicircle diameters. This improvement is attributed to the rapid formation of a dense Ca–P-enriched surface layer that synergistically stabilizes the underlying TiO_2 passive film.

After 14 days of immersion in SBF, the TH composite exhibited a total interfacial resistance of approximately 16 MΩ.cm^2, confirming the development of a highly resistive, multilayered passive/apatite structure that effectively suppresses charge transfer and ionic diffusion. In contrast, the Ti–ZrO_2 composite (TZ) showed delayed but noticeable improvement in corrosion resistance over prolonged immersion,

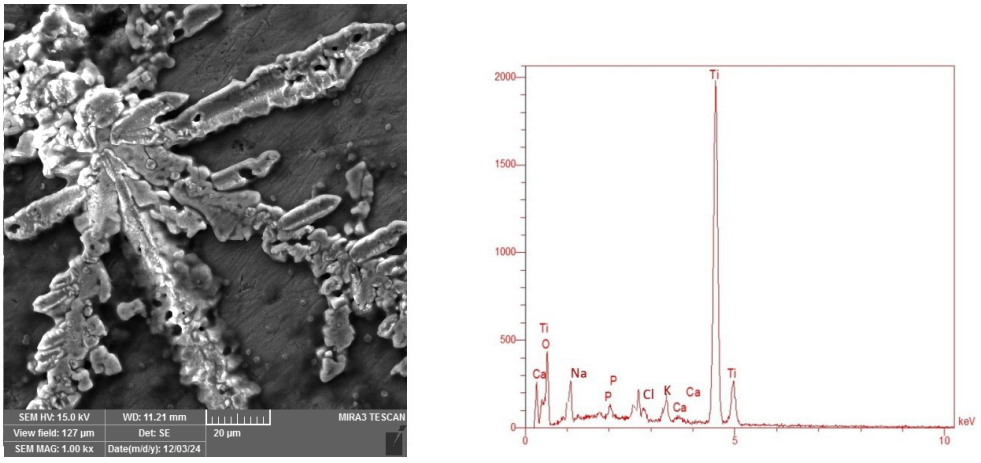

Fig. 15. SEM image of the surface of the TH sample in SBF after 14 days of immersion, along with an EDS analysis of the marked spot.

indicating that ZrO_2 contributes to long-term passivation through the gradual formation of a stable ZrO_2-rich barrier.

The dual-reinforced composite (TZH), however, displayed inferior corrosion performance compared to TH. This behavior is linked to microstructural heterogeneities, ceramic–ceramic interfacial mismatch, and the formation of electrolyte-permeable pathways that compromise passive-film integrity. These findings highlight that simultaneous addition of ZrO_2 and nHA does not necessarily produce a synergistic effect and may instead introduce structural complexity detrimental to corrosion protection.

In terms of bioactivity, the TH composite exhibited the highest density and most uniform distribution of apatite deposits after 14 days in SBF, confirming its superior ability to promote nucleation and growth of bone-like mineral phases. This enhanced bioactivity is directly related to the nanoscale HA reinforcement, which increases surface energy and provides abundant nucleation sites for Ca–P deposition.

Overall, the Ti–10 vol% nHA composite demonstrated the most balanced and superior performance, combining excellent corrosion resistance with strong in-vitro bioactivity, making it a promising candidate for long-term orthopedic implant applications. The results emphasize the critical role of nanoparticle dispersion, interfacial stability, and passive-layer evolution in determining the functional performance of Ti-based biocomposites. Future work should focus on long-term in-vitro and in−vivo evaluations to further elucidate the interfacial bonding and degradation behavior under physiological conditions.

CRediT authorship contribution statement

Shaghayegh Habibi Anganeh: Investigation, Data curation.
Vahideh Shahedifar: Project administration, Conceptualization, Writing – original draft.
Bahereh Tekyeh-Marouf: Conceptualization.

Data availability

The data underlying this article will be shared on reasonable request to the corresponding author.

Declaration of competing interest

The authors declare no competing interests.

Funding and acknowledgment

There is no external funding for this work.

References

[1] W. Abd-Elaziem, M.A. Darwish, A. Hamada, W.M. Daoush, Titanium-Based alloys and composites for orthopedic implants Applications: A comprehensive review, Mater. Des. 241 (2024) 112850. https://doi.org/10.1016/j.matdes.2024.112850.

[2] M. Abd-Elwahed, A. Ibrahim, M. Reda, Effects of ZrO2 nanoparticle content on microstructure and wear behavior of titanium matrix composite, J. Mater. Res. Technol. 9 (2020) 8528–8534. https://doi.org/10.1016/j.jmrt.2020.05.021.

[3] H. Chao, Y.-c. Li, X.-g. Liang, L.-p. Chen, Z. Na, X.-k. Zhu, Effect of composition and sintering temperature on mechanical properties of ZrO2 particulate-reinforced titanium-matrix composite, Trans. Nonferrous Met. Soc. China. 22 (2012) 1855–1859. https://doi.org/10.1016/S1003-6326(11)61397-6.

[4] F. Li, X. Jiang, Z. Shao, D. Zhu, Z. Luo, Research Progress Regarding Interfacial Characteristics and the Strengthening Mechanisms of Titanium Alloy/Hydroxyapatite Composites, Materials. 11 (2018) 1391. https://doi.org/10.3390/ma11081391.

[5] S.O. Jeje, M.B. Shongwe, A.L. Rominiyi, P.A. Olubambi, Spark plasma sintering of titanium matrix composite—a review, Int. J. Adv. Manuf. Technol. 117 (2021) 2529–2544. https://doi.org/10.1007/s00170-021-07840-7.

[6] O.E. Falodun, B.A. Obadele, S.R. Oke, A.M. Okoro, P.A. Olubambi, Titanium-based matrix composites reinforced with particulate, microstructure, and mechanical properties using spark plasma sintering technique: a review, Int. J. Adv. Manuf. Technol. 102 (2019) 1689–1701. https://doi.org/10.1007/s00170-018-03281-x.

[7] A.L. Rominiyi, P.M. Mashinini, Spark plasma sintering of discontinuously reinforced titanium matrix composites: densification, microstructure and mechanical properties—a review, Int. J. Adv. Manuf. Technol. 124 (2023) 709–736. https://doi.org/10.1007/s00170-022-10564-x.

[8] C. Ma, Y.H. Wang, M.Q. Li, L.J. Qu, Bioactivity, Wear and Corrosion Resistant Properties of Rare Earth/Calcium Phosphate Composite Coatings, Key Eng. Mater. 368–372 (2008) 1194–1197. https://doi.org/10.4028/www.scientific.net/KEM.368-372.1194.

[9] S. Kweh, K. Khor, P. Cheang, An in Vitro Investigation of Plasma Sprayed Hydroxyapatite (HA) Coatings Produced with Flame-Spheroidized Feedstock, Biomaterials. 23 (2002) 775–85. https://doi.org/10.1016/S0142-9612(01)00183-1.

[10] M. Chozhanathmisra, K. Pandian, D. Govindaraj, P. Karthikeyan, L. Mitu, R. Rajavel, Halloysite Nanotube-Reinforced Ion-Incorporated Hydroxyapatite-Chitosan Composite Coating on Ti-6Al-4 V Alloy for Implant Application, J. Chem. 2019 (2019) 7472058. https://doi.org/10.1155/2019/7472058.

[11] K. Niespodziana, K. Jurczyk, J. Jakubowicz, M. Jurczyk, Fabrication and properties of titanium–hydroxyapatite nanocomposites, Mater. Chem. Phys. 123 (2010) 160–165. https://doi.org/10.1016/j.matchemphys.2010.03.076.

[12] H. Tanigawa, H. Asoh, T. Ohno, M. Kubota, S. Ono, Electrochemical corrosion and bioactivity of titanium–hydroxyapatite composites prepared by spark plasma sintering, Corros. Sci. 70 (2013) 212–220. https://doi.org/10.1016/j.corsci.2013.01.032.

[13] F. Xie, J. Huang, S. Cao, X. He, Effects of hydroxyapatite addition on corrosion behavior and in-vitro bioactivity of Ti-10Mo matrix biocomposite, Mater. Today Commun. 31 (2022) 103787. https://doi.org/10.1016/j.mtcomm.2022.103787.

[14] E.S. Krishna G. Suresh, Bioactive titanium-hydroxyapatite composites by powder metallurgy route, Biointerface Res. Appl. Chem. 12 (2022) 5375–5383. https://doi.org/10.33263/BRIAC124.53755383.

[15] E.S. Krishna G. Suresh, Titanium-nanohydroxyapatite composites produced by ball milling and sintering: wettability, bioactivity and toxicity studies, Metall. Res. Technol. 119 (2022) 112. https://doi.org/10.1051/metal/2022005.

[16] M. Bahraminasab, M. Bozorg, S. Ghaffari, F. Kavakebian, Corrosion of Al2O3-Ti composites under inflammatory condition in simulated physiological solution, Mater. Sci. Eng: C. 102 (2019) 200–211. https://doi.org/10.1016/j.msec.2019.04.047.

[17] M. Mohammadtaheri, M. Bozorg, A. Yazdani, M. Salehi, Fabrication of Ti–Al2O3–HA composites by spark plasma sintering and its properties for medical applications, J. Mater. Res. 37 (2022) 2571–2580. https://doi.org/10.1557/s43578-022-00561-x.

[18] H.M. Yehia, A. El-Tantawy, I. Ghayad, A.S. Eldesoky, O. El-kady, Effect of zirconia content and sintering temperature on the density, microstructure, corrosion, and biocompatibility of the Ti–12Mo matrix for dental applications, J. Mater. Res. Technol. 9 (2020) 8820–8833. https://doi.org/10.1016/j.jmrt.2020.05.109.

[19] L. Brazda, D. Rohanova, A. Helebrant, Kinetics of dissolution of calcium phosphate (Ca-P) bioceramics, Process. Appl. Ceram. 2 (2008) 57–62. https://doi.org/10.2298/PAC0801057B.
[20] R. Zhao, X. Meng, Z. Pan, Y. Li, H. Qian, et al., Advancements in nanohydroxyapatite: synthesis, biomedical applications and composite developments, Regen. Biomater. 12 (2025) 129. https://doi.org/10.1093/rb/rbae129.
[21] S. Gudić, L. Vrsalović, D. Kvrgić, A. Nagode, Electrochemical Behaviour of Ti and Ti-6Al-4V Alloy in Phosphate Buffered Saline Solution, Materials. 14 (2021) 7495. https://doi.org/10.3390/ma14247495.
[22] M. Textor, C. Sittig, V. Frauchiger, S. Tosatti, D.M. Brunette, Properties and Biological Significance of Natural Oxide Films on Titanium and Its Alloys, Titanium in Medicine: Material Science, Surface Science, Engineering, Biological Responses and Medical Applications, Heidelberg: Springer, Berlin, Heidelberg. (2001) 171–230. https://doi.org/10.1007/978-3-642-56486-4_7.
[23] D.J. Patty, A.D. Nugraheni, I. Dewi Ana, Y. Yusuf, Mechanical Characteristics and Bioactivity of Nanocomposite Hydroxyapatite/Collagen Coated Titanium for Bone Tissue Engineering, Bioengineering. 9 (2022) 784. https://doi.org/10.3390/bioengineering9120784.
[24] F. Xie, Q. Sun, Y. Mu, S. Cao, G. Wu, Z. Lu, Tribological behavior and in vitro biocompatibility of powder metallurgical Ti–15Mo/HA composite for bone repair, J. Mech. Behav. Biomed. Mater. 152 (2024) 106466. https://doi.org/10.1016/j.jmbbm.2024.106466.
[25] V. Zaichick, M. Tzaphlidou, Determination of calcium, phosphorus, and the calcium/phosphorus ratio in cortical bone from the human femoral neck by neutron activation analysis, Appl. Radiat. Isot. 56 (2002) 781–786. https://doi.org/10.1016/S0969-8043(02)00066-0.